Straintronic Effect on Phonon-Mediated Superconductivity of Nb_2CT_2 (T = O, S, Se, or Te) MXenes

Sheng-Yan Wang,[1] Chen Pan,[1] Hui Tang,[1] Hong-Yun Wu,[1] Guo-Yong Shi,[1] Kun Cao,[1] Hong Jiang,[1] Yue-Hua Su,[1] Chao Zhang,[1] Kai-Ming Ho,[2] and Cai-Zhuang Wang[2, 3]*

[1] *Department of Physics, Yantai University, Yantai 264005, China*

[2] *Department of Physics and Astronomy, Iowa State University, Ames, Iowa 50011, USA*

[3] *Ames Laboratory-USDOE, Iowa State University, Ames, Iowa 50011, USA*

KEYWORDS: MXenes, superconductivity, electron-phonon coupling, strain effect, first-principles calculations

ABSTRACT: The electronic structures, phonon dispersions, and electron-phonon coupling of Nb_2CT_2 (T = O, S, Se, or Te) MXenes were investigated via first-principles calculations. Different models of Nb_2CT_2 were constructed and the results show the low-energy models of Nb_2CT_2 are intrinsic phonon-mediated superconductors. Of the four Nb_2CT_2 MXenes, Nb_2CO_2 MXene exhibits the largest superconducting critical temperature (T_c) of 14.43 K. The existence of soft modes induced by Kohn anomalies and the contribution of Nb atoms to the Fermi level lead to strong electron-phonon coupling (λ = 0.92) in Nb_2CO_2 MXene. The T_c of Nb_2CO_2 is further

enhanced by biaxial tensile strain and reaches up to 18.28 K under 4% tensile strain. The predicted T_c of Nb_2CS_2 is 4.5 K, which is comparable with experimental data. These findings will further stimulate the search for superconducting MXenes.

1. Introduction

Ultrathin two-dimensional (2D) materials have generated much interest among the scientific community due to their versatile advantageous properties that hold potential for next-generation technologies. MXene, a diverse large group of 2D materials, are especially attractive because they may serve as the building blocks for novel functional materials and new devices.[1] Since the first MXene (2D Ti_3C_2) was reported in 2011,[2] more than 30 MXenes have been experimentally synthesized and over 100 theoretically predicted.[3] The electronic structures of MXenes vary widely from metallic to insulating, and MXenes have been used to produce materials with properties relevant to a variety of applications such as energy storage,[4-7] transparent conductors and heaters,[8-11] photo-thermal therapy,[12-15] photocatalysts,[16-21] thermoelectrics,[22-26] superconductors,[27-28] ferromagnets,[29-30] topological insulators,[31-33] and more.

MXenes are generated by selectively etching the A component from the MAX phase; M indicates an early transition metal, A is an element from the third or fourth main group, and X represents carbon or nitrogen. Due to the unsaturated transition metal layer and unpaired electrons in the precursor MAX, the surface of MXenes always absorbs various functional groups, yielding the general formula $M_{n+1}X_nT_x$, where n can vary from 1 to 4 and T_x denotes the surface terminations for the outermost layers of the transition metal. The composition and configuration of the surface terminations strongly influence the physical and chemical properties of MXenes. Terminated by O (OH) and F, Nb_2CT_x MXenes have a better reversible capacity

than Ti_3C_2 and Ti_2C, making them as promising electrode materials for Li-ion batteries.[34] Furthermore, the capacity of delaminated Nb_2CT_x and carbon nanotube (CNT) composites when used as Li-ion battery electrodes are larger than that of multilayer Nb_2CT_x.[35] Nb_2C MXene covered with Nb_2O_5 can be used as a photocatalyst for hydrogen evolution, and has a better photocatalytic capacity than Nb_2O_5.[36] The structural, mechanical and electronic properties of Nb_2CCl_2 and $Nb_3C_2Cl_2$ MXenes were investigated by first-principles calculations. Both Nb_2CCl_2 and $Nb_3C_2Cl_2$ are nonmagnetic metals.[37] Recently, Kamysbayev *et al*. introduced a general strategy to modify the termination of MXenes.[38] Unexpectedly, S- and Se-terminated Nb_2C MXenes exhibit superconductivity and the superconducting critical temperatures (T_c) of Nb_2CS_2 and Nb_2CSe are 6.4 K and 4.5 K, respectively.

Inspired by the discovery of superconductivity in Nb_2CS_2 and Nb_2CSe, we systematically investigated Nb_2CT_2 (T = O, S, Se, or Te) via first-principles calculations using density functional perturbation theory. We built four structure models for each Nb_2CT_2 based on different surface termination configurations. We studied the electronic properties, thermodynamic stability, and superconducting properties of the energy-favorable structural models of Nb_2CT_2. Nb_2CO_2, Nb_2CS_2, Nb_2CSe_2, and Nb_2CTe_2 were found to exhibit superconductivity with T_c of 14.43 K, 4.54 K, 0.53 K, and 0.27 K, respectively. The T_c of Nb_2CO_2 is further enhanced by external tensile strain, and reaches 18.28 K at 4% tensile strain.

2. Computational methods

Structural optimization, electronic band structure, phonon vibration, and electron-phonon coupling calculations were conducted within the density functional perturbation theory (DFPT) framework implemented in the Quantum-Espresso (QE) package.[39] We employed the

generalized gradient approximation (GGA) exchange correlation functional of the Perdew-Burke-Ernzerhof (PBE) type and norm-conserving pseudopotentials to mimic the interactions between electrons and ions.[40-42] The kinetic energy cutoff of plane wave and charge density were taken as 80 Ry and 560 Ry, respectively. To eliminate the interlayer interaction created by the periodic boundary condition, we set the vacuum layer to 20 Å. We adopted a 12 × 12 × 1 *k*-point grid with a Gaussian smearing width of 0.02 Ry to simulate the Brillouin zone (BZ) integrations to calculate the self-consistent electron charge density. Convergence in the plane-wave basis set was confirmed by employing higher kinetic energy cutoffs. The electron-phonon coupling was checked carefully on a series *q*-point mesh and convergence was achieved with a 6 × 6 × 1 *q*-point mesh using individual electron-phonon coupling matrix elements obtained with a 12 × 12 × 1 *k*-point mesh.

3. Results and discussion

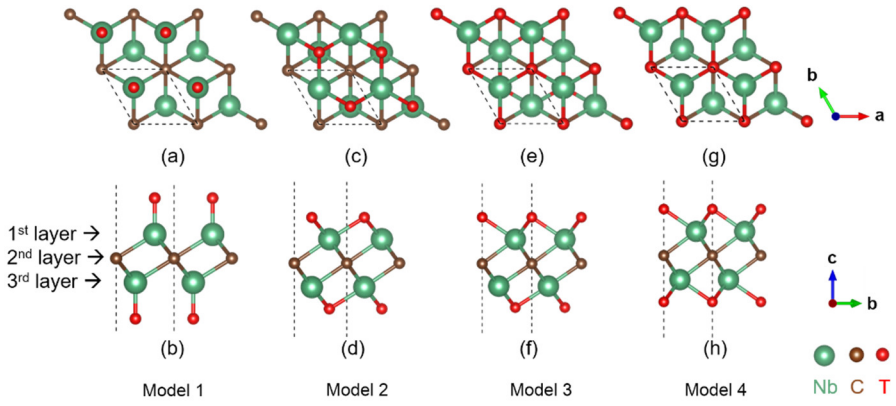

Figure. 1 Schematic diagram of Nb_2CT_2 MXenes structure. (a), (c), (e), and (g) Top view of Model 1, Model 2, Model 3, and Model 4. (b), (d), (f), and (h) Side view of Model 1, Model 2, Model 3, and Model 4. Light green, brown, and red balls represent Nb, C, and T atoms, respectively.

There are several passivated configurations for surface termination of Nb_2CT_2. Following previous work,[37, 43-44] we considered four possible surface configurations for Nb_2CT_2, as shown in Figs. 1(a)-(h), which were termed Model 1 to Model 4. An unpassivated Nb_2C system consists of three atomic layers within a hexagonal cell: two Nb layers and one C layer. In Model 1, one chalcogenide atom (T) is positioned at the top site in the first Nb layer and another T atom is positioned at the top site in the third Nb layer, as shown in Figs. 1(a) and 1(b). For Model 2, the T atom connected to the first and third Nb layer locate on the top site of the third and first Nb layer, respectively. In Model 3, the position of first T atom is similar to that of Model 2, whereas the other T atom locates on the top site of the middle C layer. In Model 4, the T atoms are located on the top site of the middle C layer on both sides, as shown in Figs. 1(g) and 1(h). Details of structural properties of these four models of Nb_2CT_2 MXenes are provided in the Supporting Information.

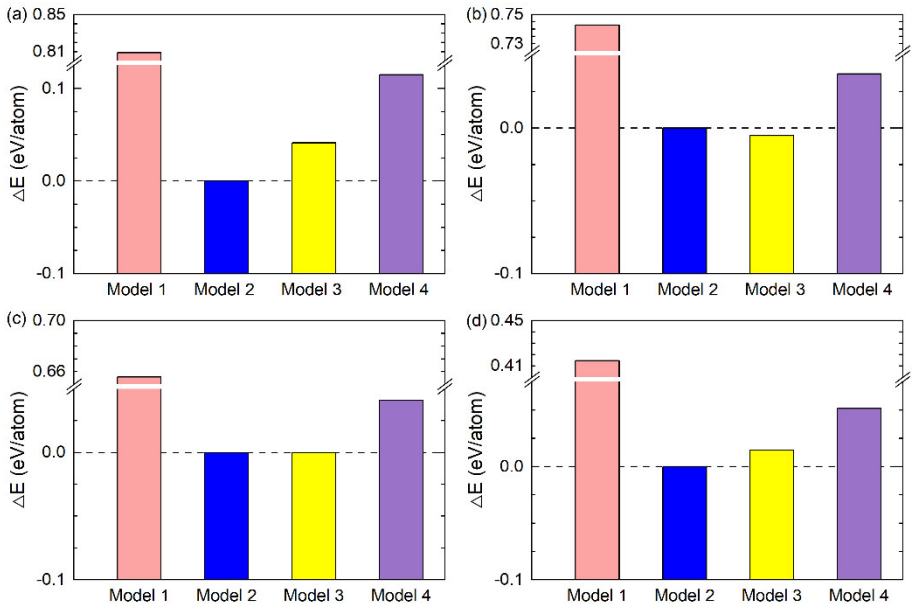

Figure. 2 Energy comparison of four models for (a) Nb_2CO_2, (b) Nb_2CS_2, (c) Nb_2CSe_2, and (d) Nb_2CTe_2. The total energy of Model 2 for each Nb_2CT_2 is set to 0.0 eV. The dash lines are guide to the eye.

After relaxing the lattice constants and the atomic positions, the relative total energies per atom for each Nb_2CT_2 MXene system are shown in Fig. 2. To clearly illustrate the energy differences, we set the total energy per atom for Model 2 of each system to be 0.0 eV. From Fig. 2, we can see that Model 2 is the most stable configuration of Nb_2CT_2 MXenes with O and Te as terminal groups, which is consistent with previous results.[37] On the other hand, Model 3 is the most stable configuration for Nb_2CT_2 MXenes with S and Se; the energy differences between Model 3 and Model 2 for the two systems are within 5 meV/atom. However, Model 3 is nonmetal, except for Nb_2CO_2 system, as shown in the Supporting Information. Therefore, we focused on Model 2 in the following study of electronic and vibrational properties and possible superconductivity.

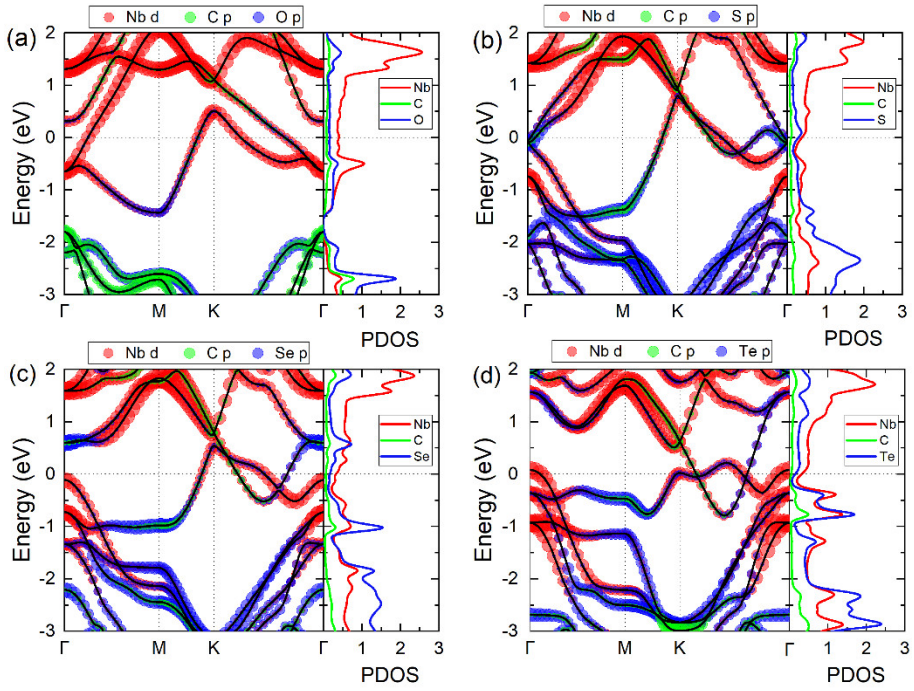

Figure. 3 Electronic orbital-resolved band structure and projected density of states of Model 2 for (a)Nb_2CO_2, (b) Nb_2CS_2, (c) Nb_2CSe_2, and (d) Nb_2CTe_2. The Fermi level indicated by the dotted line is set to 0 eV.

The electronic orbital-resolved band structures and projected density of states (PDOS) for Nb_2CT_2 are plotted in Fig. 3. Clearly, all of the Model 2 of Nb_2CT_2 are metallic with several bands crossing the Fermi level. Moreover, the orbitals from the Nb atoms mostly contribute to the DOS at the Fermi level and the smallest contribution comes from the orbitals of the C atoms. The PDOS of the Nb atom at the Fermi level of Nb_2CT_2 decrease as the mass of T atom increases. For Nb_2CO_2, the Nb 4*d* orbitals dominate the Fermi level, while the C 2*p* and O 2*p* orbitals have a limited contribution. For the Nb_2CS_2, Nb_2CSe_2, and Nb_2CTe_2 systems, there is strong hybridization between the Nb and T atoms below the Fermi level from -3 eV to -1 eV. Two bands cross the Fermi level in Nb_2CO_2, as shown in Fig. 3(a). The band crossing the Fermi level along the Γ-M and K-Γ path creates a hexagram Fermi sheet around the Γ center, whereas the band crosses the Fermi level along the M-K and K-Γ path forms a K-centered electron pocket, which corresponds to an arc-type Fermi sheet surrounding the vertexes of the first BZ, as shown in Fig. 4(a). Compared with Nb_2CO_2, more bands cross the Fermi level in Nb_2CS_2. These bands form four types of Fermi sheet, i.e., two Γ-centered circles, six ellipses along the Γ-K path, and six arcs around the K vertexes. The six arc Fermi sheets around the K vertexes have relatively large Fermi velocities, as shown in Fig. 4(b). The electronic band structure of Nb_2CSe_2 is similar to that of Nb_2CS_2 in the vicinity of the Fermi level, except for the two bands around the Γ point, which result in a relatively simple Fermi surface for Nb_2CSe_2 (Fig. 4c). For Nb_2CTe_2, three bands cross the Fermi level, as shown in Fig. 3(d). These crossing bands form a Γ-centered electron pocket and two Dirac cones along the Γ-K path, and most of these bands are flat and thus result in a low Fermi velocity, as shown in Fig. 4(d).

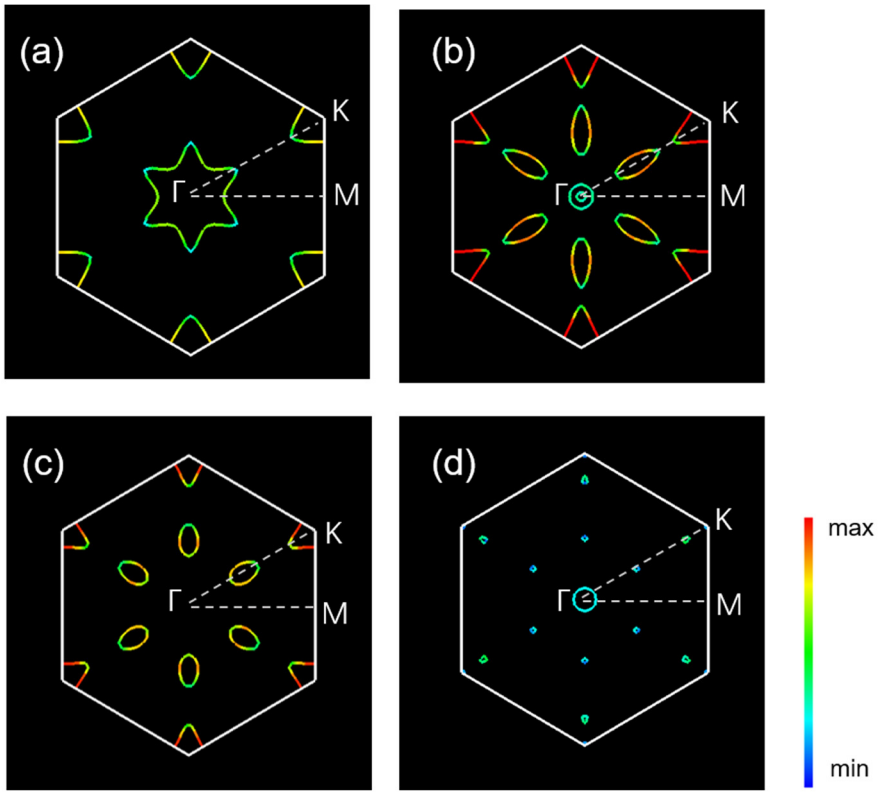

Figure. 4 Fermi surface in the first Brillouin zone of Model 2 for (a) Nb_2CO_2, (b) Nb_2CS_2, (c) Nb_2CSe_2, and (d) Nb_2CTe_2. The variation of the color of the Fermi sheet is proportional to the magnitude of the Fermi velocity.

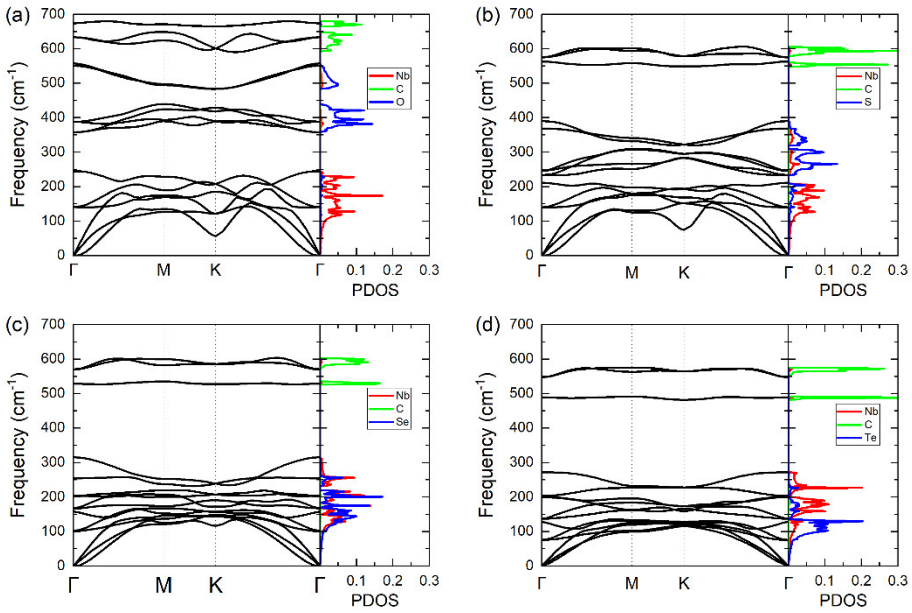

Figure. 5 Phonon dispersion and projected density of states of Model 2 for (a) Nb_2CO_2, (b) Nb_2CS_2, (c) Nb_2CSe_2, and (d) Nb_2CTe_2.

Figure 5 presents the phonon spectrum and phonon projected density of states of Nb_2CT_2 MXenes. The absence of imaginary phonon frequencies confirm that these 2D Nb_2CT_2 systems are thermodynamically stable and could be synthesized under appropriate experimental conditions. The phonon spectra of Nb_2CO_2 and Nb_2CS_2 are distinctly different to the two other systems. The vibration frequencies of Nb_2CO_2 and Nb_2CS_2 can be divided into three parts, i.e., the low-, intermediate-, and high-frequency ranges. For Nb_2CO_2, the low-frequency range (below 250 cm^{-1}), intermediate-frequency range (350 ~ 550 cm^{-1}), and high-frequency range (above 600 cm^{-1}) are respectively dominated by Nb, O, and C atoms. Due to the large atomic mass of S, the intermediate-frequency vibration moves downward, which enhances the interaction between the Nb and S atoms, especially from 150 cm^{-1} to 400 cm^{-1}. The T-related frequency range moves further downward in the Nb_2CSe_2 and Nb_2CTe_2 systems, which leads to disappearance of the intermediate-range frequency. It is noteworthy that there is a dip in the phonon dispersion curve around the K point of the first BZ of Nb_2CT_2 MXenes, as shown in Fig. 5. This soft phonon mode at the K point is known as Kohn anomaly.[45-48] The Kohn anomaly is due to anomalous screening of the electrons around the Fermi level and further yields significant coupling between electrons and phonons. It occurs in a particular wave vector of phonon q in the BZ, which connects two electronic states on the Fermi surface: k and k', satisfying $k' = k + q$. The Kohn anomaly take places at the K point for an acoustic phonon mode with a low frequency of ~ 57 cm^{-1}, ~ 75 cm^{-1}, and ~ 116 cm^{-1} for Nb_2CO_2, $Nb2CS_2$, and $Nb2CSe_2$ MXenes, respectively. The Kohn anomaly is apparent in Nb_2CO_2 and $Nb2CS_2$, and becomes weaker in Nb_2CSe_2, and then not present in Nb_2CTe_2.

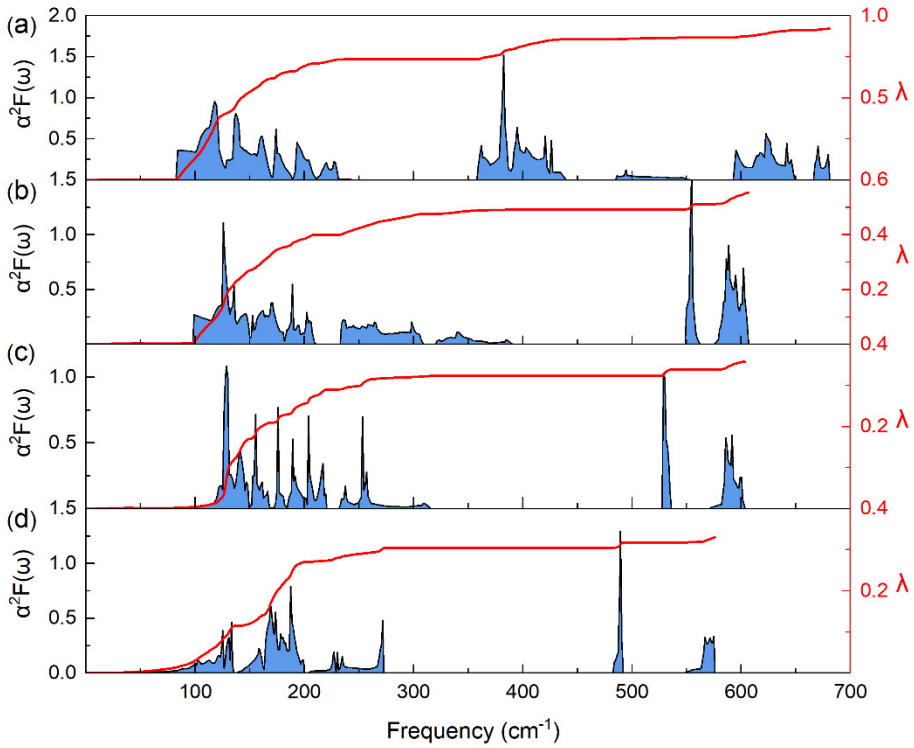

Figure. 6 Eliashberg spectral function $\alpha^2F(\omega)$ and frequency-dependent integrated electron-phonon coupling constant $\lambda(\omega)$ for (a) Nb_2CO_2, (b) Nb_2CS_2, (c) Nb_2CSe_2, and (d) Nb_2CTe_2.

The Eliashberg spectral function, $\alpha^2F(\omega)$, and integrated electron-phonon coupling constant, $\lambda(\omega)$, are presented in Fig. 6. Similarly to the phonon PDOS, the distribution of $\alpha^2F(\omega)$ in Nb_2CO_2 and Nb_2CS_2 are different to that of the Nb_2CSe_2 and Nb_2CTe_2 systems. Nb_2CO_2 possesses the largest integrated electron-phonon coupling of 0.92 of the four systems. The low-frequency (Nb-dominated) range, intermediate-frequency (O-dominated) range, and high-frequency (C-dominated) range contribute 79.6%, 13.3%, and 7.1% of the total λ, respectively. Nb_2CS_2 has a relatively small λ (0.55). The contribution of phonon vibration to the total λ is similar in Nb_2CS_2 and Nb_2CO_2. Nb_2CSe_2 and Nb_2CTe_2 have small λ, as shown in Table 1. Vibration of Nb and T atoms contribute 90.3% and 92.2% of the total λ for Nb_2CSe_2 and Nb_2CTe_2, respectively. The large λ of Nb_2CO_2 motivates us to reinspect the Fermi surface and phonon dispersion. We found that the

large arc-type Fermi sheet around the K point and the apparent Kohn anomaly at the K point of first BZ for Nb_2CO_2. Thus, the coupling between the electrons coming from the arc-type Fermi sheet and the softening phonon modes induced by Kohn anomaly results to a large λ. Moreover, the above mentioned electrons and phonon modes mainly come from Nb atoms, which is consistent with the analysis of Eliashberg spectral function.

Table. 1 Logarithmic average frequency $\omega_{\log}$, electron-phonon coupling constant λ, and superconducting critical temperature T_c for four Nb_2CT_2 MXenes.

	$\omega_{\log}$ (K)	λ	T_c (K)
Nb_2CO_2	236.51	0.92	14.43
Nb_2CS_2	258.60	0.55	4.54
Nb_2CSe_2	254.74	0.36	0.53
Nb_2CTe_2	237.45	0.33	0.27

According to the Allen-Dynes modified version of the McMillan equation:[49-50]

$$T_c = \frac{\omega_{log}}{1.2}\exp\left[-\frac{1.04(1+\lambda)}{\lambda-\mu^*(1+0.62\lambda)}\right]$$

we estimated the T_c of Nb_2CT_2 using the Coulomb pseudopotential $\mu^* = 0.10$, as shown in Table 1. Clearly, Nb_2CO_2 possesses the largest T_c (14.43 K) of the four Nb_2CT_2 MXenes systems, while Nb_2CTe_2 has a relatively small T_c of 0.27 K. It is worth noting that the reported T_c of Nb_2CS_2 is 6.4 K, which is good agreement with our theoretical data (4.54 K).[38] We note that superconductivity was not experimentally observed in Nb_2CO_2, probably as the experimental sample had a different structure to that used in the present calculations. The experimental sample

was cold-pressed pellets, while the present theoretical calculations were based on a multilayer atomic structure of only five angstroms thickness.

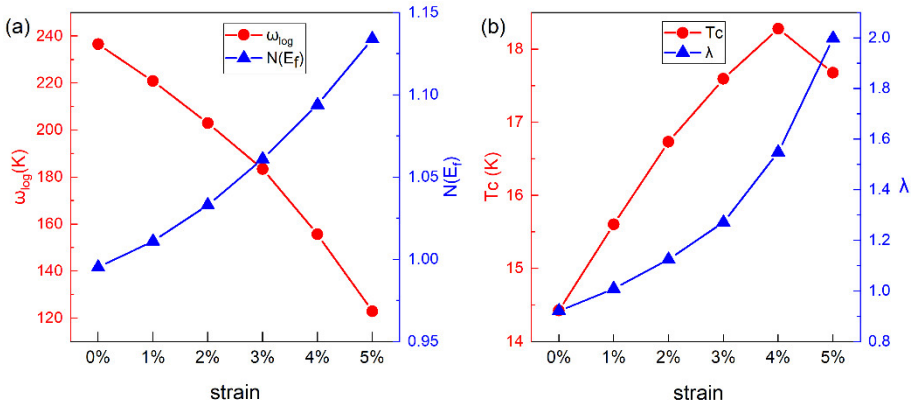

Figure. 7 Effect of biaxial strain on (a) ω_{log} and $N(E_f)$, and (b) λ and T_c for Nb_2CO_2.

Stain has been proved to be an effective approach to tune electronic and dynamic properties of 2D materials.[51-57] Introducing strain is a mature and important technology in nanomaterials, as well as MXenes.[58-59] The strain effects on the superconductivity of 2D materials have been extensively investigated theoretically within the framework of BCS theory.[47, 60-67] The superconductivity was predicted to be enhanced by biaxial strain in some 2D materials, such as 2D phosphorus carbide[47] and 2D tungsten boride.[63] Here, we introduced biaxial strain to the Nb_2CO_2 MXene, which has the largest T_c in the absence of strain among the four systems, and investigated the strain effects on superconductivity. Biaxial strain (δ) ranging from -5% to 5% was applied to Nb_2CO_2 at intervals of 1% to simulate the conditions of sample growth on a substrate. δ was calculated as $\delta = (a - a_0)/a_0$, where a_0 is the lattice constant in the absence of strain, and negative and positive values indicate compressive and tensile strain, respectively. Imaginary phonon frequencies were observed for Nb_2CO_2 under -5% to -1% strain, which means that compressive strain destroys the stability of Nb_2CO_2 MXene. Figure 7 presents the variations in the superconductivity-related parameters of

Nb_2CO_2 under tensile strain. Interestingly, the λ and DOS at the Fermi level $N(E_f)$ increase monotonically with tensile strain, whereas the ω_{log} decreases monotonically with tensile strain. Due to interplay between ω_{log}, λ, and $N(E_f)$, the T_c of Nb_2CO_2 initially increases with tensile stain and reaches 18.28 K at 4% strain, and then decreases to 17.68 K at 5% tensile strain. In addition to biaxial strain, we also applied uniaxial or shear strains on the Nb_2CO_2 MXene; however, most of the configurations of Model 2 of Nb_2CO_2 MXene under uniaxial or shear strains become thermodynamically unstable. Therefore, we focused on biaxial strain and explored the mechanism of strain effects on superconductivity in the following text.

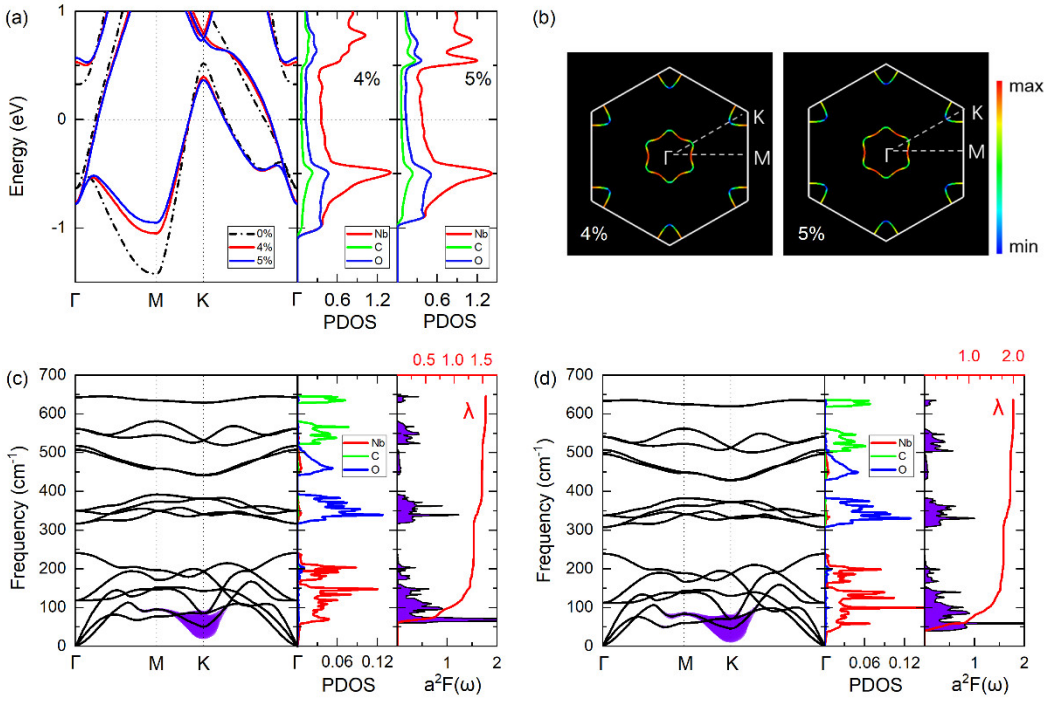

Figure. 8 (a) Electronic band structure and PDOS, (b) Fermi surface of Nb_2CO_2 MXenes under tensile strain. EPC-weighted phonon spectra, Phonon PDOS, $\alpha^2F(\omega)$ and frequency-dependent integrated $\lambda(\omega)$ of Nb_2CO_2 MXenes under (c) 4% and (d) 5% strain. The weight in the phonon

spectrum is proportional to the electron-phonon coupling strength λ_{qv}, marked in purple. The subscript *q* represents the wave vector and *v* represents the phonon mode.

Figure 8 shows the electronic and thermodynamic properties of Nb_2CO_2 under 4% and 5% tensile strain. The electronic bands that cross the Fermi level become slightly smoother, as shown in Fig. 8(a). The contribution of Nb atoms to the Fermi level increases as the strain increases. The shapes of the Fermi surface of Nb_2CO_2 under 0%, 4%, and 5% strain are similar, as shown in Fig. 8(b). Under 4% and 5% tensile strain, the intermediate-frequency and high-frequency phonon vibrations for Nb_2CO_2 move downward, and the low-frequency range (Nb-dominated) remains below 250 cm^{-1}. This leads to a decrease in ω_{log}. The low-lying vibration mode controlled by Nb atoms contributes 86.4% and 88.9% of total λ, respectively. The projected λ_{qv} shows the soft mode at the K point contributes significantly to the total λ. Between 0% and 4% strain, the increase in λ correlates with $N(E_f)$ and dominates the increase in the T_c of Nb_2CO_2. Between 4% and 5% strain, the reduction in ω_{log} originates from the downshift of the phonon vibrations under tensile strain, and overcomes the increase in λ and eventually decreases the T_c of Nb_2CO_2 under 5% strain.

4. Conclusions

In summary, the electronic and superconducting properties of Nb_2CT_2 (T = O, S, Se, or Te) MXenes were investigated using first-principles calculations within the DFPT framework. We built four structural models for each Nb_2CT_2 MXene based on different surface passivations, and then focused on the low-energy Model 2. Nb_2CO_2 possesses a strong electron-phonon coupling (λ = 0.92), which leads to the largest T_c among the four Nb_2CT_2 MXenes. The existence of soft modes due to Kohn anomalies and the contribution from Nb atoms to the Fermi level account for the strong electron-phonon coupling of Nb_2CO_2. Using the Allen and Dynes modified McMillan

equation, we calculated the T_c of Nb_2CO_2 is to be 14.43 K. Furthermore, the T_c of Nb_2CO_2 is enhanced by tensile strain and increases by 27% at 4% tensile strain. At 5% tensile strain, T_c decreases to 17.68 K due to reduction of ω_{log} of phonon vibrations overcoming the increase in electron-phonon coupling. The results have great implications for the superconductivity of MXenes and other 2D systems.

ASSOCIATED CONTENT

Supporting Information.

The Supporting Information is available free of charge on the ACS Publications website.

Details of structural parameters, superconducting critical temperature, electronic band structures, and phonon spectrum of Nb_2CT_2 MXenes. (PDF)

AUTHOR INFORMATION

Corresponding Author

*E-mail : phyczhang@ytu.edu.cn

Author Contributions

The manuscript was written through contributions of all authors. All authors have given approval to the final version of the manuscript.

ORCID

Chao Zhang: 0000-0002-5957-2287

Hong Jiang: 0000-0003-0143-0056

Cai-Zhuang Wang: 0000-0002-0269-4785

Notes

The authors declare no competing financial interest.

ACKNOWLEDGMENT

This work was supported by the National Natural Science Foundation of China (Grants Nos. 11874318 and 11774299), the Natural Science Foundation of Shandong Province (Grants Nos. ZR2018MA043 and ZR2017MA033). Work at Ames Laboratory was supported by the U.S. Department of Energy, Office of Science, Basic Energy Sciences, Division of Materials Science and Engineering including the computer time support came from National Energy Research Scientific Computing Center (NERSC) in Berkeley, CA. Ames Laboratory is operated for the U.S. DOE by Iowa State University under Contract No. DE-AC02-07CH11358.

REFERENCES

1. Gogotsi, Y.; Huang, Q., MXenes: Two-Dimensional Building Blocks for Future Materials and Devices. *ACS Nano* **2021**, *15*, 5775-5780.
2. Naguib, M.; Kurtoglu, M.; Presser, V.; Lu, J.; Niu, J.; Heon, M.; Hultman, L.; Gogotsi, Y.; Barsoum, M. W., Two-Dimensional Nanocrystals Produced by Exfoliation of Ti_3AlC_2. *Adv. Mater.* **2011**, *23*, 4248-4253.
3. Anasori, B.; Gogotsi, Û. G., *2D Metal Carbides and Nitrides (MXenes) Structure, Properties and Applications*; Springer: Cham, Switzerland, 2019.
4. Peng, Y.-Y.; Akuzum, B.; Kurra, N.; Zhao, M.-Q.; Alhabeb, M.; Anasori, B.; Kumbur, E. C.; Alshareef, H. N.; Ger, M.-D.; Gogotsi, Y., All-MXene (2D Titanium Carbide) Solid-State Microsupercapacitors for on-Chip Energy Storage. *Energy Environ. Sci.* **2016**, *9*, 2847-2854.
5. Garg, R.; Agarwal, A.; Agarwal, M., A Review on MXene for Energy Storage Application: Effect of Interlayer Distance. *Mater. Res. Express* **2020**, *7*, 022001.
6. Yang, Y.; Chen, J.; Tang, J.; Xing, F.; Yao, M., Investigation on the Structure–Performance Correlation of TiC MXenes as Cathode Catalysts for Li-O_2 Batteries. *J. Phys. Chem. C* **2021**, *125*, 21453-21459.
7. Siriwardane, E. M. D.; Demiroglu, I.; Sevik, C.; Peeters, F. M.; Çakır, D., Assessment of Sulfur-Functionalized MXenes for Li-ion Battery Applications. *J. Phys. Chem. C* **2020**, *124*, 21293-21304.
8. Mariano, M.; Mashtalir, O.; Antonio, F. Q.; Ryu, W.-H.; Deng, B.; Xia, F.; Gogotsi, Y.; Taylor, A. D., Solution-Processed Titanium Carbide MXene Films Examined as Highly

Transparent Conductors. *Nanoscale* **2016**, *8*, 16371-16378.
9. Ying, G.; Kota, S.; Dillon, A. D.; Fafarman, A. T.; Barsoum, M. W., Conductive Transparent V_2CT_x (MXene) Films. *FlatChem* **2018**, *8*, 25-30.
10. Zhang, C. J.; Nicolosi, V., Graphene and MXene-Based Transparent Conductive Electrodes and Supercapacitors. *Energy Storage Mater.* **2019**, *16*, 102-125.
11. Park, T. H.; Yu, S.; Koo, M.; Kim, H.; Kim, E. H.; Park, J.-E.; Ok, B.; Kim, B.; Noh, S. H.; Park, C., Shape-Adaptable 2D Titanium Carbide (MXene) Heater. *ACS Nano* **2019**, *13*, 6835-6844.
12. Yu, X.; Cai, X.; Cui, H.; Lee, S.-W.; Yu, X.-F.; Liu, B., Fluorine-Free Preparation of Titanium Carbide MXene Quantum Dots with High near-Infrared Photothermal Performances for Cancer Therapy. *Nanoscale* **2017**, *9*, 17859-17864.
13. Szuplewska, A.; Kulpińska, D.; Dybko, A.; Jastrzębska, A. M.; Wojciechowski, T.; Rozmysłowska, A.; Chudy, M.; Grabowska-Jadach, I.; Ziemkowska, W.; Brzózka, Z., 2D Ti_2C (MXene) as a Novel Highly Efficient and Selective Agent for Photothermal Therapy. *Mat. Sci. Eng. C* **2019**, *98*, 874-886.
14. Huang, Z.; Cui, X.; Li, S.; Wei, J.; Li, P.; Wang, Y.; Lee, C.-S., Two-Dimensional MXene-Based Materials for Photothermal Therapy. *Nanophotonics* **2020**, *9*, 2233-2249.
15. Liu, Y.; Han, Q.; Yang, W.; Gan, X.; Yang, Y.; Xie, K.; Xie, L.; Deng, Y., Two-Dimensional MXene/Cobalt Nanowire Heterojunction for Controlled Drug Delivery and Chemo-Photothermal Therapy. *Mat. Sci. Eng. C* **2020**, *116*, 111212.
16. Guo, Z.; Zhou, J.; Zhu, L.; Sun, Z., MXene: A Promising Photocatalyst for Water Splitting. *J. Mater. Chem. A* **2016**, *4*, 11446-11452.
17. Cheng, L.; Li, X.; Zhang, H.; Xiang, Q., Two-Dimensional Transition Metal MXene-Based Photocatalysts for Solar Fuel Generation. *J. Phys. Chem. Lett* **2019**, *10*, 3488-3494.
18. Kuang, P.; Low, J.; Cheng, B.; Yu, J.; Fan, J., MXene-Based Photocatalysts. *J. Mater. Sci. Technol.* **2020**, *56*, 18-44.
19. Xie, X.; Zhang, N., Positioning MXenes in the Photocatalysis Landscape: Competitiveness, Challenges, and Future Perspectives. *Adv. Funct. Mater.* **2020**, *30*, 2002528.
20. Pandey, M.; Thygesen, K. S., Two-Dimensional MXenes as Catalysts for Electrochemical Hydrogen Evolution: A Computational Screening Study. *J. Phys. Chem. C* **2017**, *121*, 13593-13598.
21. Wei, B.; Fu, Z.; Legut, D.; Germann, T. C.; Zhang, Q.; Du, S.; Zhang, H.; Francisco, J. S.; Zhang, R., Two-Dimensional Carbonitride MXenes as an Efficient Electrocatalyst for Hydrogen Evolution. *J. Phys. Chem. C* **2021**, *125*, 4477-4488.
22. Khazaei, M.; Arai, M.; Sasaki, T.; Estili, M.; Sakka, Y., Two-Dimensional Molybdenum Carbides: Potential Thermoelectric Materials of the MXene Family. *Phys. Chem. Chem. Phys* **2014**, *16*, 7841-7849.
23. Gandi, A. N.; Alshareef, H. N.; Schwingenschlögl, U., Thermoelectric Performance of the MXenes M_2CO_2 (M = Ti, Zr, or Hf). *Chem. Mater.* **2016**, *28*, 1647-1652.
24. Kumar, S.; Schwingenschlögl, U., Thermoelectric Performance of Functionalized Sc_2C MXenes. *Phys. Rev. B* **2016**, *94*, 035405.
25. Sarikurt, S.; Çakır, D.; Keçeli, M.; Sevik, C., The Influence of Surface Functionalization on Thermal Transport and Thermoelectric Properties of MXene Monolayers. *Nanoscale* **2018**, *10*, 8859-8868.
26. Jing, Z.; Wang, H.; Feng, X.; Xiao, B.; Ding, Y.; Wu, K.; Cheng, Y., Superior Thermoelectric Performance of Ordered Double Transition Metal MXenes: $Cr_2TiC_2T_2$ (T = −Oh or −F). *J. Phys. Chem. Lett* **2019**, *10*, 5721-5728.

27. Lei, J.; Kutana, A.; Yakobson, B. I., Predicting Stable Phase Monolayer Mo_2C (MXene), a Superconductor with Chemically-Tunable Critical Temperature. *J. Mater. Chem. C* **2017**, *5*, 3438-3444.
28. Bekaert, J.; Sevik, C.; Milošević, M. V., First-Principles Exploration of Superconductivity in MXenes. *Nanoscale* **2020**, *12*, 17354-17361.
29. Yue, Y., Fe2c Monolayer: An Intrinsic Ferromagnetic MXene. *J. Magn. Magn. Mater.* **2017**, *434*, 164-168.
30. Frey, N. C.; Kumar, H.; Anasori, B.; Gogotsi, Y.; Shenoy, V. B., Tuning Noncollinear Spin Structure and Anisotropy in Ferromagnetic Nitride MXenes. *ACS Nano* **2018**, *12*, 6319-6325.
31. Weng, H.; Ranjbar, A.; Liang, Y.; Song, Z.; Khazaei, M.; Yunoki, S.; Arai, M.; Kawazoe, Y.; Fang, Z.; Dai, X., Large-Gap Two-Dimensional Topological Insulator in Oxygen Functionalized MXene. *Phys. Rev. B* **2015**, *92*, 075436.
32. Liang, Y.; Khazaei, M.; Ranjbar, A.; Arai, M.; Yunoki, S.; Kawazoe, Y.; Weng, H.; Fang, Z., Theoretical Prediction of Two-Dimensional Functionalized MXene Nitrides as Topological Insulators. *Phys. Rev. B* **2017**, *96*, 195414.
33. Balcı, E.; Akkuş, Ü. Ö.; Berber, S., Controlling Topological Electronic Structure of Multifunctional MXene Layer. *Appl. Phys. Lett.* **2018**, *113*, 083107.
34. Naguib, M.; Halim, J.; Lu, J.; Cook, K. M.; Hultman, L.; Gogotsi, Y.; Barsoum, M. W., New Two-Dimensional Niobium and Vanadium Carbides as Promising Materials for Li-ion Batteries. *J. Am. Chem. Soc.* **2013**, *135*, 15966-15969.
35. Mashtalir, O.; Lukatskaya, M. R.; Zhao, M.-Q.; Barsoum, M. W.; Gogotsi, Y., Amine-Assisted Delamination of Nb_2c MXene for Li-ion Energy Storage Devices. *Adv. Mater.* **2015**, *27*, 3501-3506.
36. Su, T.; Peng, R.; Hood, Z. D.; Naguib, M.; Ivanov, I. N.; Keum, J. K.; Qin, Z.; Guo, Z.; Wu, Z., One-Step Synthesis of Nb_2O_5/C/Nb_2C (MXene) Composites and Their Use as Photocatalysts for Hydrogen Evolution. *ChemSusChem* **2018**, *11*, 688-699.
37. Qin, Y.; Zha, X.-H.; Bai, X.; Luo, K.; Huang, Q.; Wang, Y.; Du, S., Structural, Mechanical and Electronic Properties of Two-Dimensional Chlorine-Terminated Transition Metal Carbides and Nitrides. *J. Phys.:Condens. Matter* **2020**, *32*, 135302.
38. Kamysbayev, V.; Filatov, A. S.; Hu, H.; Rui, X.; Lagunas, F.; Wang, D.; Klie, R. F.; Talapin, D. V., Covalent Surface Modifications and Superconductivity of Two-Dimensional Metal Carbide MXenes. *Science* **2020**, *369*, 979.
39. Giannozzi, P.; Baroni, S.; Bonini, N.; Calandra, M.; Car, R.; Cavazzoni, C.; Ceresoli, D.; Chiarotti, G. L.; Cococcioni, M.; Dabo, I., et al., Quantum Espresso: A Modular and Open-Source Software Project for Quantum Simulations of Materials. *J. Phys.:Condens. Matter* **2009**, *21*, 395502.
40. Perdew, J. P.; Burke, K.; Ernzerhof, M., Generalized Gradient Approximation Made Simple. *Phys. Rev. Lett.* **1996**, *77*, 3865-3868.
41. Troullier, N.; Martins, J. L., Efficient Pseudopotentials for Plane-Wave Calculations. *Phys. Rev. B* **1991**, *43*, 1993.
42. Fuchs, M.; Scheffler, M., Ab Initio Pseudopotentials for Electronic Structure Calculations of Poly-Atomic Systems Using Density-Functional Theory. *Comput. Phys. Commun.* **1999**, *119*, 67-98.
43. Khazaei, M.; Arai, M.; Sasaki, T.; Chung, C.-Y.; Venkataramanan, N. S.; Estili, M.; Sakka, Y.; Kawazoe, Y., Novel Electronic and Magnetic Properties of Two-Dimensional Transition Metal Carbides and Nitrides. *Adv. Funct. Mater.* **2013**, *23*, 2185-2192.

44. Zha, X.-H.; Luo, K.; Li, Q.; Huang, Q.; He, J.; Wen, X.; Du, S., Role of the Surface Effect on the Structural, Electronic and Mechanical Properties of the Carbide MXenes. *EPL-Europhys. Lett.* **2015**, *111*, 26007.
45. Kohn, W., Image of the Fermi Surface in the Vibration Spectrum of a Metal. *Phys. Rev. Lett.* **1959**, *2*, 393.
46. Caruso, F.; Hoesch, M.; Achatz, P.; Serrano, J.; Krisch, M.; Bustarret, E.; Giustino, F., Nonadiabatic Kohn Anomaly in Heavily Boron-Doped Diamond. *Phys. Rev. Lett.* **2017**, *119*, 017001.
47. Wang, B.-T.; Liu, P.-F.; Bo, T.; Yin, W.; Eriksson, O.; Zhao, J.; Wang, F., Superconductivity in Two-Dimensional Phosphorus Carbide (β_0-PC). *Phys. Chem. Chem. Phys* **2018**, *20*, 12362-12367.
48. Piscanec, S.; Lazzeri, M.; Mauri, F.; Ferrari, A.; Robertson, J., Kohn Anomalies and Electron-Phonon Interactions in Graphite. *Phys. Rev. Lett.* **2004**, *93*, 185503.
49. McMillan, W. L., Transition Temperature of Strong-Coupled Superconductors. *Phys. Rev.* **1968**, *167*, 331.
50. Allen, P. B.; Dynes, R. C., Transition Temperature of Strong-Coupled Superconductors Reanalyzed. *Phys. Rev. B* **1975**, *12*, 905.
51. Lu, A. J.; Zhang, R. Q.; Lee, S. T., Stress-Induced Band Gap Tuning in <112> Silicon Nanowires. *Appl. Phys. Lett.* **2007**, *91*, 263107.
52. Hong, K.-H.; Kim, J.; Lee, S.-H.; Shin, J. K., Strain-Driven Electronic Band Structure Modulation of Si Nanowires. *Nano Lett.* **2008**, *8*, 1335-1340.
53. Zhang, C.; De Sarkar, A.; Zhang, R. Q., Strain Induced Band Dispersion Engineering in Si Nanosheets. *J. Phys. Chem. C* **2011**, *115*, 23682-23687.
54. Guo, Z.; Miao, N.; Zhou, J.; Sa, B.; Sun, Z., Strain-Mediated Type-I/Type-II Transition in MXene/Blue Phosphorene Van Der Waals Heterostructures for Flexible Optical/Electronic Devices. *J. Mater. Chem. C* **2017**, *5*, 978-984.
55. Siriwardane, E. M. D.; Karki, P.; Loh, Y. L.; Çakır, D., Strain–Spintronics: Modulating Electronic and Magnetic Properties of $Hf_2mnc_2o_2$ MXene by Uniaxial Strain. *J. Phys. Chem. C* **2019**, *123*, 12451-12459.
56. Li, S.-S.; Li, X.-H.; Zhang, R.-Z.; Cui, H.-L., Strain-Tunable Electronic Properties and Optical Properties of Hf_2CO_2 MXene. *Int. J. Quantum. Chem.* **2020**, *120*, e26365.
57. Lu, W.; Zhai, H.; Li, Q.; Chen, C., Pronounced Enhancement of Superconductivity in ZrN Via Strain Engineering. *J. Phys. Chem. Lett* **2021**, *12*, 1985-1990.
58. Zhu, Y.; Liu, J.; Guo, T.; Wang, J. J.; Tang, X.; Nicolosi, V., Multifunctional $Ti_3C_2T_x$ MXene Composite Hydrogels with Strain Sensitivity toward Absorption-Dominated Electromagnetic-Interference Shielding. *ACS Nano* **2021**, *15*, 1465-1474.
59. Seyedin, S.; Uzun, S.; Levitt, A.; Anasori, B.; Dion, G.; Gogotsi, Y.; Razal, J. M., MXene Composite and Coaxial Fibers with High Stretchability and Conductivity for Wearable Strain Sensing Textiles. *Adv. Funct. Mater.* **2020**, *30*, 1910504.
60. Ge, Y.; Wan, W.; Yang, F.; Yao, Y., The Strain Effect on Superconductivity in Phosphorene: A First-Principles Prediction. *New J. Phys.* **2015**, *17*, 035008.
61. Zeng, S.; Zhao, Y.; Li, G.; Ni, J., Strongly Enhanced Superconductivity in Doped Monolayer MoS_2 by Strain. *Phys. Rev. B* **2016**, *94*, 024501.
62. Li, G.; Zhao, Y.; Zeng, S.; Zulfiqar, M.; Ni, J., Strain Effect on the Superconductivity in Borophenes. *J. Phys. Chem. C* **2018**, *122*, 16916-16924.
63. Yan, L.; Bo, T.; Zhang, W.; Liu, P.-F.; Lu, Z.; Xiao, Y.-G.; Tang, M.-H.; Wang, B.-T., Novel

Structures of Two-Dimensional Tungsten Boride and Their Superconductivity. *Phys. Chem. Chem. Phys* **2019**, *21*, 15327-15338.
64. Yan, L.; Liu, P.-F.; Li, H.; Tang, Y.; He, J.; Huang, X.; Wang, B.-T.; Zhou, L., Theoretical Dissection of Superconductivity in Two-Dimensional Honeycomb Borophene Oxide B_2O Crystal with a High Stability. *npj Comput. Mater.* **2020**, *6*, 94.
65. Yan, L.; Bo, T.; Liu, P.-F.; Zhou, L.; Zhang, J.; Tang, M.-H.; Xiao, Y.-G.; Wang, B.-T., Superconductivity in Predicted Two Dimensional XB_6 (X = Ga, In). *J. Mater. Chem. C* **2020**, *8*, 1704-1714.
66. Bo, T.; Liu, P.-F.; Yan, L.; Wang, B.-T., Electron-Phonon Coupling Superconductivity in Two-Dimensional Orthorhombic MB_6 (M = Mg, Ca, Ti, Y) and Hexagonal MB_6 (M = Mg, Ca, Ti, Y) *Physical Review Materials* **2020**, *4*, 114802.
67. Yan, L.; Liu, P.-F.; Bo, T.; Zhang, J.; Tang, M.-H.; Xiao, Y.-G.; Wang, B.-T., Emergence of Superconductivity in a Dirac Nodal-Line Cu_2Si Monolayer: Ab Initio Calculations. *J. Mater. Chem. C* **2019**, *7*, 10926-10932.